# Coupled spatial multimode solitons in microcavity wires

G. Slavcheva,[1,*] A. V. Gorbach,[1] and A. Pimenov[2]
[1]*Department of Physics, University of Bath, Bath, BA2 7AY, United Kingdom*
[2]*Weierstrass Institute, Mohrenstrasse 39, D-10117 Berlin, Germany*
(Received 2 August 2016; published 23 December 2016)

A modal expansion approach is developed and employed to investigate and elucidate the nonlinear mechanism behind the multistability and formation of coupled multimode polariton solitons in microcavity wires. With pump switched on and realistic dissipation parameters, truncating the expansion up to the second-order wire mode, our model predicts two distinct coupled soliton branches: stable and unstable. Modulational stability of the stationary homogeneous solution and soliton branches stability are studied. Our simplified 1D model is in remarkably good agreement with the full 2D mean-field Gross-Pitaevskii model, reproducing correctly the soliton existence domain upon variation of pump amplitude and the onset of multistability.

DOI: 10.1103/PhysRevB.94.245432

## I. INTRODUCTION

Future advances in optical quantum information processing will require development of 'on chip' capabilities. Integrated optical technologies for quantum computing based on linear optics have been under active development in the recent decade [1]. However, nonlinear optical interactions 'on a chip' are largely unexplored and may play a key role.

Nonlinear interactions with microcavity exciton-polaritons (entangled light-matter states that result from strong coupling of the quantum well exciton to the microcavity photons) are particularly attractive candidate for physical implementation of polaritonic integrated circuits 'on a chip' [2,3], owing to a number of advantages intrinsic to this system, compared to bare photons and excitons alone. Due to the excitonic component, exciton-polaritons exhibit weaker diffraction than the photons and can be confined within structures with submicron size. The strong interparticle interactions result in very strong and fast low-threshold optical nonlinearities [4] arising from parametric scattering of exciton-polaritons [5,6], driven by Coulomb exchange interaction and phase-space filling [7]. On the other hand, owing to their photon component, exciton-polaritons are extremely light particles, which allows build-up of many-body coherent effects such as Bose-Einstein condensation (BEC) [8], suggesting the possibility of creating a polariton condensate at high temperatures.

Recently a number of nonlinear self-localisation phenomena with microcavity polaritons in strongly-coupled planar quantum well semiconductor microcavities have been demonstrated, such as bright [9] and dark hydrodynamic polariton solitons [10], superfluidity [11], pattern formation [12,13], vortices [14,15] and self-organisation of vortices and antivortices in lattices [16,17]. In open dissipative systems, when the dispersion and decay of the polariton wave packets is balanced by the nonlinearity and pump, a nonlinear mode that travels undistorted forms, known as polariton soliton. We note that there exists a quantum-classical correspondence between the collective fluid dynamics of a Bose-Einstein polariton condensate and a polariton soliton. Polariton BEC is a spontaneous quantum phase transition driven by quantum fluctuations, resulting in momentum space polariton localisation, as opposed to dissipative solitons that are classical localized structures in real space. These classical localized entities may be formed by different mechanisms, such as resonant coherent pump and a superimposed seed (or random classical noise) stimulation in the optical parametric triggered regime, by non-resonant incoherent pump excitation in the presence of a saturable absorber [18], or inhomogeneous pumps and/or trapping potentials [19]. For instance, it has been recently demonstrated [18] that dissipative polariton solitons may exist both in the presence of Kerr-like (parametric polariton) nonlinearity and in its absence. In the quantum case, the exciton-polariton condensate flows without friction and thus can be viewed as a 'quantum soliton'. In what follows, we are going to consider dissipative solitons in the coherent triggered optical parametric oscillator regime.

Optical bistability is yet another manifestation of microcavity polariton nonlinearity. When the excitation laser is blue-detuned with respect to the lower polariton (LP) branch the response of the excited mode becomes bistable in a finite range of excitation powers. When sweeping the excitation power forward and backward, an hysteresis curve is observed that arises from Kerr-like nonlinearity induced by polariton-polariton interactions [20]. The optical polarization (spinor) multistability of microcavity polaritons has been extensively studied both theoretically [21–24] and experimentally [25–29]. It has been theoretically demonstrated [30] that multistability in a multicomponent polaritonic fluid can be realized either by two coherent pumps, or considering the polarization degree of freedom. Polariton bistability associated with parametric scattering processes under incoherent pumping has been demonstrated theoretically [31] and experimentally [32].

When two or more stationary stable states coexist, a different kind of optical multistability – spatial multistability – takes place, characterized by specific transverse spatial profiles, with one-to-one correspondence to each of the stable states of the optical multistability curve. This phenomenon has been initially discussed in the context of mode competition, transverse laser dynamics and pattern formation in a laser cavity [33]. Recently spatial multistability has been demonstrated experimentally using 3D-confined 0-dimensional microcavity

*g.slavcheva@bath.ac.uk

 

exciton-polaritons in patterned mesas (polariton quantum boxes) [34]. It has been shown that the spatial profile of the transmitted beam is determined by the lateral confinement of the optical modes. This multimode interacting system has been described by an extension to multimodes of the mean-field spinor Gross-Pitaevskii equations [35] in a exciton-photon basis.

In a recent work [36] we found composite 'multimode' polariton solitons in 1D microcavity wires [37], particularly promising building blocks for planar polaritonic integrated circuits, that result from the superposition of the fundamental and multiple higher-order co-existing transverse cavity modes. Unlike single-mode polariton soliton solutions previously found in planar semiconductor microcavities that are stable within the bistability domain, the multimode solitons exhibit more complex multistable behavior. Polariton soliton formation is based on self-localisation phenomena triggered by modulational instabilities and in this respect, it resembles the pattern formation due to transverse instability in a resonantly pumped planar microcavity, discussed in [38,39]. The spatial multistability does not involve polariton spin degree of freedom and differs from both the polarization multistability, and the spatial multistability described in [34]. While there is one-to-one correspondence between the transverse modes in a 0-D polariton quantum box and the stable states in the multistability curve in [34], there is no such one-to-one correspondence between the transverse modes and the stable states (branches) in the multistability curve of a 1D microcavity wire: the polariton mode gradually reshapes and evolves when sweeping the pump amplitude along a given stable branch.

In this study, we shall focus on the bright multimode polariton solitons and the associated multistable behavior. We shall show that this peculiar type spatial multistability and the multimode polariton solitons, that can be supported by it, requires development of a multimode model, similar to [34]. The 2D mean-field Gross-Pitaevskii is a generic model, which encapsulates the correct dispersion of all polaritonic modes in the wire, however it conceals all the details of inter-modal nonlinear interactions within the "convoluted envelope" form. In particular, it fails to explain the observed spatial multistability, the multimode polariton soliton domains of existence and the peculiar non-monotonous soliton velocity behavior in microcavity wires with different widths [40]. Therefore, the 2D model does not provide important parameters that can be externally controlled and modified to achieve control over the multimode interactions and polariton dynamics.

In order to get a deeper insight into the soliton solutions we need to go beyond the two-mode description within the driven-dissipative Gross-Pitaevskii equations. We develop a modal expansion method, expanding the nonlinear polariton modes in the basis of free polariton modes. The multimode analysis helps to investigate in detail conditions, dynamics and stability of coupled soliton formation and identify reliably ranges of soliton existence.

The 1D reduced coupled-mode model, that we develop in this paper, provides fundamental understanding of the nonlinear mechanisms behind these interactions and means for control e.g. through the polariton dispersion. Understanding and exercising such control holds benefits for the fabrication technologies targeting novel polaritonic integrated devices based on structured microcavities [37,41]. Furthermore, our approach permits to describe some soliton branches, such as multihumped soliton branches, which are otherwise hard to find by a straightforward numerical propagation in the 2D model. In addition, finding and analyzing numerically exact solitons as stationary solutions, e.g. by Newton-Raphson method, also proves to be a hard task within the 2D model. For such tasks, our derived coupled-modes model offers a significant advantage.

Another motivation for the present work comes from the generally unsolved problem of understanding nonlinear pulse propagation in multimode systems, such as optical fibres, nonlinear optical and polaritonic waveguides. The latter has become a topic of considerable interest in view of pushing the inherent limits for information transmission of the communication technologies by space-division multiplexing, exploiting multiple spatial transverse mode channels, and high-speed applications, such as all-optical switching using ultrashort high peak power pulses. Several experiments have demonstrated that there is also significant potential for new spatial and spectral nonlinear effects in multimode fibers [42,43] and nonlinear waveguides [44].

Self-localisation optical phenomena in multimode systems are possible as a result of counter-balancing of a combination of dispersive effects: (i) material dispersion, due to frequency-dependent dielectric response; (ii) waveguide modes dispersion; (iii) variation of the group velocity of each waveguide mode, and nonlinearity. For instance in optical fibres, 'complex envelope' multimode solitons have been theoretically predicted in the early 80*s* [45–47] and only very recently experimentally studied [48,49]. Nonlinear localization effects such as 'soliton trapping' [50] has recently been theoretically demonstrated whereby two solitons in different modes shift their spectra and travel at the same speed in spite of considerable intermodal differential group delay between them. For third-order nonlinear processes such as four-photon mixing, which are not automatically phase matched, it is possible to use the dispersion of the waveguide modes to compensate for material group dispersion in such a way as to achieve phase matching. This has been demonstrated by the observation of four-photon mixing in a multimode fibre [51]. In multimode systems the dominant dispersive effect originates from the difference in the group velocity of each excited mode. Under suitable conditions, the different modes interact among themselves in such a way as to give rise to a self-localization mechanism, due to nonresonant (intermodal cross-phase modulation through Kerr nonlinearity) and/or resonant (four-wave mixing) nonlinearities [50] that prevents the pulse from broadening as a consequence of modal dispersion [47].

In this work we show that a similar nonlinear self-confinement mechanism takes place when a light-matter wave polariton soliton, rather than an optical soliton, propagates in a microcavity wire. Self-localized light-matter wave packets in multimode polariton systems result from compensation of the polariton modes dispersion and group velocity dispersion of each cavity mode with nonlinearity. A new nonlinearity component is the intermodal nonlinear

coupling that arises from intermodal cross-phase modulation (through Kerr nonlinearity) and polariton parametric scattering (polariton four-wave mixing). Hence, multimode polariton solitons can be viewed as resulting from distribution of the excitation energy over multiple spatial modes and consisting of synchronized, nondispersive pulses in multiple spatial modes, interacting via parametric polariton nonlinearity. Here, the dominant dispersive effect originates from the difference in the group velocity of each excited cavity polariton mode.

On the other hand, polariton propagation in multimode systems is an interplay of complex nonlinear spatiotemporal phenomena and waveguide imperfections: The pulse effective coherence length is reduced from the strictly infinite coherence length of perfect phase matching by waveguide imperfections. In a parametric scattering process the pump can be either redistributed between several different polariton modes and the Stokes signal appears in one of these modes while anti-Stokes appears in a different mode, or the pump photons can be in the same mode. These two cases are referred to as "mixed-mode pump" and "single-mode pump" processes. It has been demonstrated that mixed-mode pump processes result in pulses that have much longer coherence lengths than single-mode pump processes [52]. This is a key reason for the interest in multimode polariton solitons, as they are expected to be more robust and able to propagate over much longer distances without being destroyed in a realistic waveguide with imperfections. Furthermore, as has been pointed out in Ref. [49], they are expected to exhibit novel spatiotemporal dynamics and, like single-mode solitons, may provide a convenient framework for understanding more complex nonlinear phenomena in confined multimode polariton systems.

The paper is organized as follows: We derive the modal equations, starting from the mean-field driven-dissipative Gross-Pitaevskii model, compute the multistability curves with parameters taken from Ref. [36], and perform stability analysis of the stationary homogeneous nonlinear solution in Sec. II. The coupled polariton soliton branches are computed in Sec. III for nonzero pump and realistic dissipation. Stability analysis of the soliton solutions is performed, identifying stable and unstable soliton branches. In Sec. IV we compare our 1D reduced model with the full model by reconstructing the 2D soliton from the stable soliton profiles of the first two even modes and by projecting the full-model solutions onto these modes. Finally, we compare the domain of soliton existence predicted from our reduced model with the one inferred from the full 2D mean-field model and show remarkably good agreement between the two.

## II. MODAL EQUATIONS

The starting point is our mean-field driven-dissipative Gross-Pitaevskii model [36] in a tilted along the wire reference frame, in which, for the sake of generality, we introduce inclined at an angle $\alpha$ to the channel pump with in-plane wave vector components, $q_x = q\cos(\alpha)$ $q_y = q\sin(\alpha)$ [Fig. 1(a)]:

$$i\partial_t E + \left[(\partial_x + iq_x)^2 + \partial_y^2\right]E + [i\gamma_c + \delta_c + U(y)]E + \Omega_R(y)\psi = iE_p e^{iq_y y - i\Delta t}, \tag{1}$$

$$i\partial_t \Psi + (i\gamma_e + \delta_e)\psi + \Omega_R(y)E = |\psi|^2\psi, \tag{2}$$

where $E$ and $\Psi$ are the averages of the photon and exciton creation or annihilation operators, the normalization is such that $(\omega_R/g)|E|^2$ and $(\omega_R/g)|\Psi|^2$ are the photon and exciton numbers per unit area, $g$ is the strength of exciton-exciton interaction [9], $E_p$ is the normalized pump amplitude, $\omega_R$ is the Rabi frequency in a planar homogeneous cavity, and time is measured in the units of $T = 1/\omega_R$. The unit length, $L = \sqrt{\hbar/(2m_c\omega_R)}$, is determined by the effective cavity photon mass $m_c$; $\delta_e$,$\delta_c$, and the pump frequency $\Delta$ are detunings from a reference frequency. The lateral confinement in the cavity plane (along the $y$ axis) is described by an effective potential $U(y)$ in the photonic component and a spatially confined normalized coupling $\Omega_R(y)$:

$$U(y) = U_{bg}\left[1 - e^{-(2y/w)^8}\right], \quad \Omega_R(y) = e^{-(2y/w)^8}, \tag{3}$$

where $w$ is the dimensionless wire width. As demonstrated in our previous work [36], the above super-Gaussian potentials give an accurate description of the dispersion of the lowest five guided modes of the wire.

We describe the multistable behavior of homogeneous solutions, and the apparent multimode structure of the numerically observed solitons in Ref. [36], as the result of interplay between the external pump, loss, and nonlinear interactions between multiple guided modes of the wire. In other words,

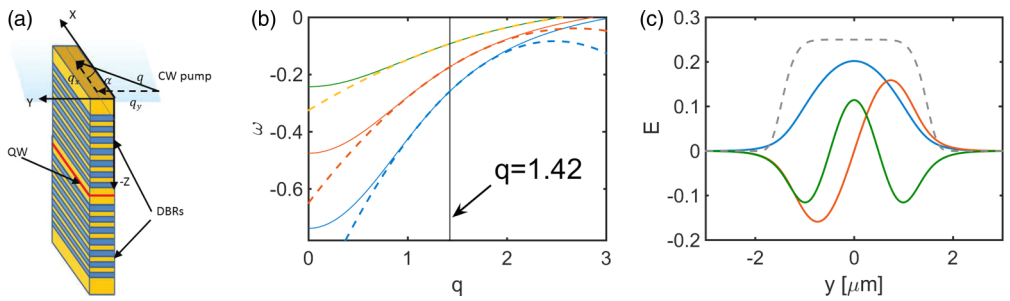


FIG. 1. (a) Scheme of the microcavity polaritonic wire structure with a tilted in-plane cw pump; (b) linear polariton dispersion with parabolic fit (dashed curves): All parameters are as in Ref. [36], and coefficients for parabolic fits are listed in Appendix B, Eqs. (B1)–(B3). (c) Modal profiles for $q = 1.4237$ (which corresponds to pump inclination at 20 degrees). All modes are normalized such that $N_j = 1$ in Eq. (6). Dashed curve indicates scaled profile of the potential $\Omega_R(y)$.

we treat nonlinearity, pump, and dissipation as perturbations and expand the solutions in free polariton modes with slowly varying amplitudes $F_j$:

$$[E,\psi]^T = \vec{x} = \sum_j \int \left[ s\frac{1}{N_j} F_j(t,k)\vec{x}_j(y,k) + s^3 \vec{B}_j(t,y,k) + O(s^5) \right] e^{ikx - i\omega_j(k)t} dk. \quad (4)$$

Here $s$ is a dummy small parameter, we assume $\partial_t F \sim sF \sim \gamma_{c,e} \sim |E_p| \ll \delta_{c,e} F$, the specific hierarchy of perturbation terms in the above ansatz is justified by solving consistently and successively the resulting equations in different orders of the small parameter $s$. We introduce optional normalization factors $N_j$ to be specified below, $\vec{B}_j$ describe corrections to the free polariton mode profiles induced by the nonlinearity. In the lowest order $O(s)$ the eigenvalue problem for free polariton modes $\vec{x}_j = [x_{je}, x_{j\psi}]^T$ of the wire is obtained:

$$\begin{bmatrix} -(q_x + k)^2 + \partial_y^2 + \delta_c + U(y) + \omega & \Omega_R(y) \\ \Omega_R(y) & \delta_e + \omega \end{bmatrix} \vec{x} = \hat{L}(k)\vec{x} = 0. \quad (5)$$

Solving this eigenvalue problem we obtain a discrete set of modes and the corresponding frequencies $\omega = \omega_j(k)$ [Fig. 1(b)]. It is convenient to normalize modes as:

$$N_j^2 = \int |\vec{x}_j|^2 dy = \int (|x_{je}|^2 + |x_{j\psi}|^2) dy. \quad (6)$$

In the next order ($s^3$) the following set of equations is obtained:

$$\sum_j \left\{ i\frac{1}{N_j}\partial_t F_j \vec{x}_j + \hat{L}(k)\vec{B}_j + i\frac{1}{N_j}\begin{bmatrix} \gamma_c x_{je} \\ \gamma_e x_{j\psi} \end{bmatrix} F_j \right\} e^{-i\omega_j(k)t} = \vec{R}$$

$$\vec{R} = \begin{bmatrix} i\delta(k) E_p e^{iq_y y - i\Delta t} \\ \sum_{lmn} \iint dk_1 dk_2 \left\{ \frac{x_{l\psi} x^*_{m\psi} x_{n\psi}}{N_l N_m N_n} F_l(k_1) F^*_m(k_2) F_n(k_3) e^{-i\omega_l t + i\omega_m t - i\omega_n t} \right\} \end{bmatrix}, \quad (7)$$

$$k_3 = k - k_1 + k_2.$$

where in the r.h.s. $\delta(k)$ stands for Dirac delta function, $\omega_l = \omega_l(k_1)$, $\omega_m = \omega_m(k_2)$, $\omega_n = \omega_n(k_3)$. Projecting these equations onto $\vec{x}_j$, using the self-adjoint properties of the operator $\hat{L}(k)$, and performing inverse Fourier transform, we finally obtain the modal equations for amplitudes $Q_j(x,t) = F_j(k,t)e^{-i\omega_j(k)t + i\Delta t}$:

$$i\partial_t Q_j + (\Delta - \omega_{j0} + i\gamma_0) Q_j + i\omega_{j1}\partial_x Q_j + \frac{\omega_{j2}}{2}\partial_x^2 Q_j = \sum_{lmn} \Gamma_{lmn,j} Q_l Q_m^* Q_n + i h_j, \quad (8)$$

where $\omega_{jl} = d^l \omega_k / dk^l$ is the Taylor expansion coefficients of the dispersion functions $\omega_j(k)$, assuming relatively narrowband excitations only terms up to $\omega_{j2}$ are retained [see dashed curves in Fig. 1(b)], and the following set of parameters is introduced:

$$h_j = \frac{1}{N_j} \int E_p e^{iq_y y} x^*_{je}(y) dy, \quad (9)$$

$$\gamma_j = \frac{1}{N_j^2} \int [\gamma_c |x_{je}|^2 + \gamma_e |x_{j\psi}|^2] dy, \quad (10)$$

$$\Gamma_{lmn,j} = \frac{1}{N_j N_l N_m N_n} \int x_{l\psi} x^*_{m\psi} x_{n\psi} x^*_{j\psi} dy. \quad (11)$$

The physical meaning of the above parameters is as follows: $h_j$ is the pump projection onto $j$th eigenmode; $\gamma_j$ are normalized dissipation parameters, and $\Gamma_{lmn,j}$ are the intermodal nonlinear coupling coefficients.

Below we shall focus on the case when the pump inclination is aligned with the orientation of the wire, i.e., $\alpha = 0$. In this case, only symmetric eigenmodes (i.e., $j = 0,2,4,\ldots$) will be excited by the homogeneous pump (see Appendices A and B). Choosing parameters of the model as in Ref. [36], we calculate dispersion and profiles of the linear modes [Figs. 1(b) and 1(c)] and hence obtain numerical values of all the parameters in the modal Eqs. (8), given in Appendix B.

To check the validity of our approach, in Fig. 2 the multistability of the homogeneous solution is illustrated for two different frequencies $\Delta$: below and above the eigenfrequency $\omega_{20}$ (Appendix B). The stationary homogeneous solution of

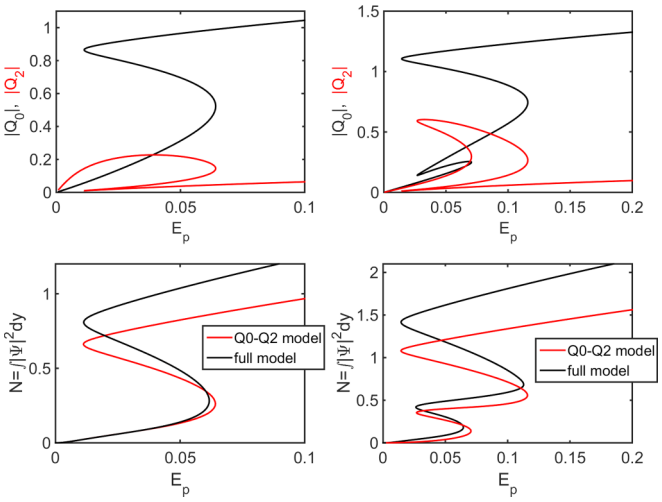


FIG. 2. Bi- and multistability of the homogeneous solution for $\gamma = 0.01$, $\Delta = -0.1$ (left column) and $\Delta = 0$ (right column), cf. Figs. 2(b) and 2(c) in Ref. [36]. Solution in terms of $Q_0$ and $Q_2$ is shown in the top row, and the corresponding conversion in terms of the full $\Psi$ field is illustrated in the bottom row ($\Psi$-norm, $N = \int |\Psi|^2 dy$).

Eqs. (8) was computed by setting all derivatives in $x$ coordinate to zero and considering only two lowest modes $Q_0$ and $Q_2$ (see top row in Fig. 2). It was then converted to the full $E$ and $\Psi$ fields according to Eq. (4) and compared against stationary solutions of the full model in Eqs. (1) and (2). Transition from bi- to multistable behavior upon variation of the detuning $\Delta$ is observed as in Figs. 2(b) and 2(c) in Ref. [36]. Discrepancy between the reduced and the full model is noticeable at high amplitudes, where inclusion of higher order modes $(Q_4, Q_6, \dots)$ is necessary. Also, in this regime nonlinear corrections to the modal amplitudes (self-defocusing) become noticeable, and therefore calculations of $\vec{B}_j(y)$ and the account of higher-order terms in the perturbation expansion may be required.

We perform next stability analysis of the multistability curves, obtained for the stationary homogeneous nonlinear solution (see Appendix C) for two pump detunings $\Delta = -0.1$ and $\Delta = 0$ and a realistic dissipation parameter $\gamma = 0.04$. This step is necessary as it provides background for analysis of the soliton solutions, which we shall compute in the following section.

## III. COUPLED SOLITON FAMILIES WITH NONZERO PUMP AND DISSIPATION

In this section we calculate the coupled soliton branches as a function of the pump amplitude for a dissipation parameter $\gamma = 0.04$ and detunings $\Delta = -0.1$ and $\Delta = 0$. We solve self-consistently Eqs. (8) for the $(Q_0, Q_2)$ coupled soliton in a moving with the soliton reference frame, introducing additional unknown parameter: the soliton velocity $u$. Two types of stable and unstable solitons are found, which we will refer to as type 1 and 2 (soliton branch stability investigated below).

The stable soliton type 1 branch is found from the final evolved profiles of the time-dependent equations [Eqs. (1) and (2)], solved by Fourier split-step method (see Ref. [36]), taken as initial guess for the Newton-Raphson method. The unstable type 2 soliton branch is obtained numerically from the coupled $(Q_0, Q_2)$ stationary equations setting initially $Q_2 = 0$ with nonzero pump terms, $h_0, h_2$. Both type 1 and 2 soliton branches are shown in Fig. 3(a) for zero detuning, $\Delta = 0$, superimposed on the homogeneous solution multistability curves. Type 1 $Q_0$ and $Q_2$ soliton branches are displayed by thick red/blue lines, respectively. In what follows we shall show that the solitons along these branches are stable. The corresponding soliton type 2 branches are denoted by solid red/blue lines. The transition between the unstable and stable branches is clearly visible by the kink in the curve. We note that there is also a gap between these two types of soliton branches, a discussion of which we will postpone to Sec. IV C.

The soliton profiles for the $Q_0$ and $Q_2$ components along the branches are shown in Figs. 3(b)–3(g) for different pump amplitudes, sweeping the curve from the left edge of the stable type 1 soliton branch up to the right edge of the unstable (type 2) branch. We note that the stable solitons (type 1) sit on a stable background of the homogeneous solution (see black portions of the curves in Fig. 3(a)) and the soliton profile remains unchanged as in Fig. 3(b) along the stable branch. By contrast, the unstable soliton type 2 sits on a modulationally unstable homogeneous solution background and this soliton profile significantly changes when sweeping the unstable branch from the left edge [Fig. 3(c)] to the right edge [Fig. 3(g)] where higher-amplitude oscillations appear in the soliton tail.

The soliton branches for the stable (type 1) and unstable solitons (type 2) merge for $\Delta = -0.1$ and $\gamma_0 = 0.04$ and are plotted in Fig. 4. The solitons are very close to stable at the left edge of the soliton branch and become more unstable towards the right edge, where the background is modulationally unstable. This is confirmed by our stability analysis of the soliton branches below.

We should note that the $Q_2$ soliton component of the stable soliton in Fig. 3(b) at $\Delta = 0, \gamma_0 = 0.04$ intersects the $Q_0$ one, thereby contributing to the specific spatial dynamics of the reconstructed 2D soliton shown in Figs. 9(a)–9(c), namely the $Q_0$ component dominates the soliton core, while the $Q_2$ component dominates the tail behavior, leading to the characteristic split double-lobe tail in transverse to the propagation direction. By contrast, in the case $\Delta = -0.1, \gamma_0 = 0.04$, the $Q_2$ component contributes to the soliton core but hardly has any influence on the soliton tail, thus leading to the single-lobe 2D spatial profile of the soliton tail, observed in Figs. 10(a)–10(c).

We perform stability analysis of the soliton solutions in a moving with the soliton frame. Introducing a new variable, $\eta = \xi - ut$, the $Q_0$ and $Q_2$ components of the coupled soliton can be written as:

$$\begin{aligned} Q_0(\eta) &= A_0(\xi - ut) = A_0(\eta) \\ Q_2(\eta) &= A_2(\xi - ut) = A_2(\eta). \end{aligned} \tag{12}$$

Adding small perturbations to the soliton profiles Eqs. (12), according to:

$$\begin{aligned} Q_0(\eta) &= A_0(\eta) + \varepsilon_f(\eta) e^{(\lambda - i\delta)t} + \varepsilon_b^*(\eta) e^{(\lambda + i\delta)t} \\ Q_2(\eta) &= A_2(\eta) + p_f(\eta) e^{(\lambda - i\delta)t} + p_b^*(\eta) e^{(\lambda + i\delta)t} \end{aligned} \tag{13}$$

and introducing linear operators: $\hat{\mathcal{L}}_j = \Delta - \omega_{j0} + i\gamma_0 + i(v_j - u)\partial_\xi + \frac{d_j}{2}\partial_\xi^2$ for $j = 0,2$, and $v_0 = 0$, we obtain the following eigenvalue problem:

$$(\delta + i\lambda)\vec{x} = \begin{bmatrix} -\hat{\mathcal{L}}_0 + 2(\Gamma_{00}|A_0|^2 + \Gamma_{20}|A_2|^2) & \Gamma_{00}A_0^2 & 2\Gamma_{20}A_0A_2^* & 2\Gamma_{20}A_0A_2 \\ -\Gamma_{00}(A_0^*)^2 & \hat{\mathcal{L}}_0^* - 2(\Gamma_{00}|A_0|^2 + \Gamma_{20}|A_2|^2) & -2\Gamma_{20}A_0^*A_2^* & -2\Gamma_{20}A_0^*A_2 \\ 2\Gamma_{02}A_0^*A_2 & 2\Gamma_{02}A_0A_2 & -\hat{\mathcal{L}}_2 + 2(\Gamma_{22}|A_2|^2 + \Gamma_{02}|A_0|^2) & \Gamma_{22}A_2^2 \\ -2\Gamma_{02}A_0^*A_2^* & -2\Gamma_{02}A_0A_2^* & -\Gamma_{22}(A_2^*)^2 & \hat{\mathcal{L}}_2^* - 2(\Gamma_{22}|A_2|^2 + \Gamma_{02}|A_0|^2) \end{bmatrix} \vec{x}, \tag{14}$$

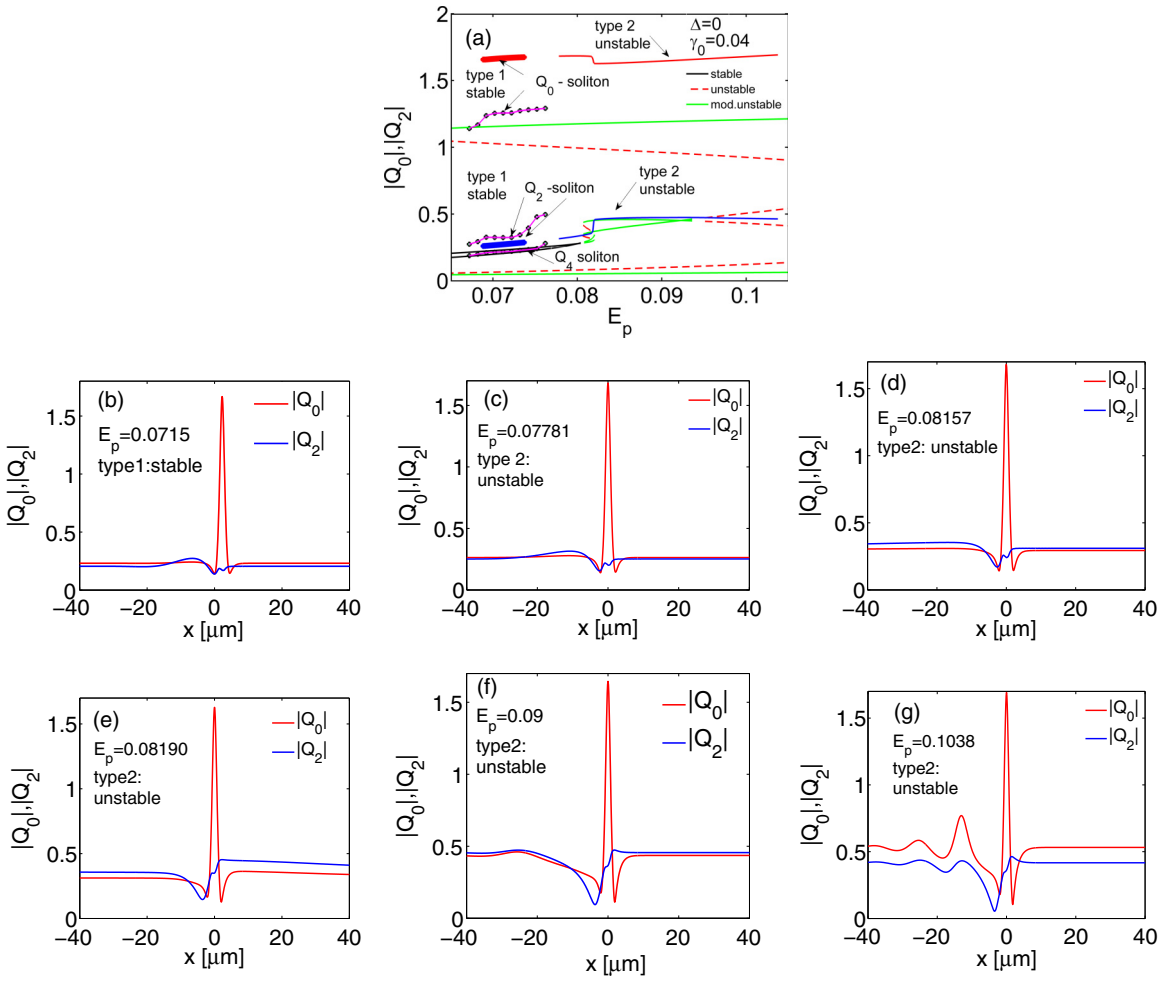


FIG. 3. (a) Coupled stable (type 1) and unstable (type 2) soliton branches, superimposed on the multistability curves of the stationary nonlinear coupled $(Q_0, Q_2)$ modes vs $E_p$ (homogeneous solution stability indicated) at $\Delta = 0$ and $\gamma_0 = 0.04$; note that the stable soliton branches sit on a stable background (black curve), while the unstable soliton branches sit on a modulationally unstable background (green curve). Soliton branches corresponding to $Q_0$, $Q_2$, and $Q_4$ soliton components, inferred from the inverse transform [Eq. (4)] of the full-model 2D solitons, computed by a dynamical (split-step) model from [Eqs. (1) and (2)], are shown with open circles connected by magenta line; (b) Stable type 1 $|Q_0|$ and $|Q_2|$-soliton profiles in the middle of the stable soliton branch at $E_p = 0.0715$; this soliton profile remains unchanged from the left stable soliton branch edge at $E_p = 0.06886$ to the right edge at $E_p = 0.07366$. Unstable type2 profiles at the (c) left edge of unstable soliton branch at $E_p = 0.07781$; (d) right edge before kink at $E_p = 0.08157$; (e) left edge after kink at $E_p = 0.08190$; (f) at $E_p = 0.09$; (g) right edge of unstable soliton branch at $E_p = 0.1038$.

The evolution of the full eigenvalue spectrum with the pump amplitude $E_p$ computed from the sparse matrix in Eq. (14) for the soliton branch at $\Delta = 0, \gamma_0 = 0.04$ is shown in Fig. 5. The solitons are stable, as all eigenvalues have negative imaginary part ($\lambda < 0$) up to a pump amplitude of $E_p = 0.073665$, corresponding to the right edge of the stable type 1 soliton branch [see Figs. 3(a)–3(c)]. Above this pump amplitude the soliton branch type 2 is unstable (since eigenvalue imaginary part, $\lambda > 0$ for at least one eigenvalue).

The full eigenvalue spectrum computed from the sparse matrix in Eq. (14) for the soliton branch at $\Delta = -0.1$, $\gamma_0 = 0.04$, for a range of pump amplitudes, starting from the left edge of the soliton branch (at $E_p = 0.039882$) and sweeping the branch up to $E_p = 0.066993$ is shown in Fig. 6. The solitons are slightly unstable towards the left edge of the soliton branch, since at least one of the eigenvalues is positive, although very close to zero, and remain slightly unstable towards the right edge.

## IV. COMPARISON WITH THE FULL MODEL

In this section we compare our reduced 1D model with the full 2D model [36]. We solve the time-dependent full-model Eqs. (1) and (2) by Fourier split-step technique, taking as initial guess the lower bistability branch homogenous solution for pump amplitude $E_p = 0.0672$, applying a seed pulse with amplitude $E_s = 0.34114$ and sweeping the whole soliton branch. The resulting evolved 3D soliton profiles are displayed in Fig. 7 at the left ($E_p = 0.0672$) and right ($E_p = 0.0762$) edge of the upper and lower soliton branches. We should note that our dynamical simulation predicts two types of solitons as the pump amplitude is increased, namely a single-hump

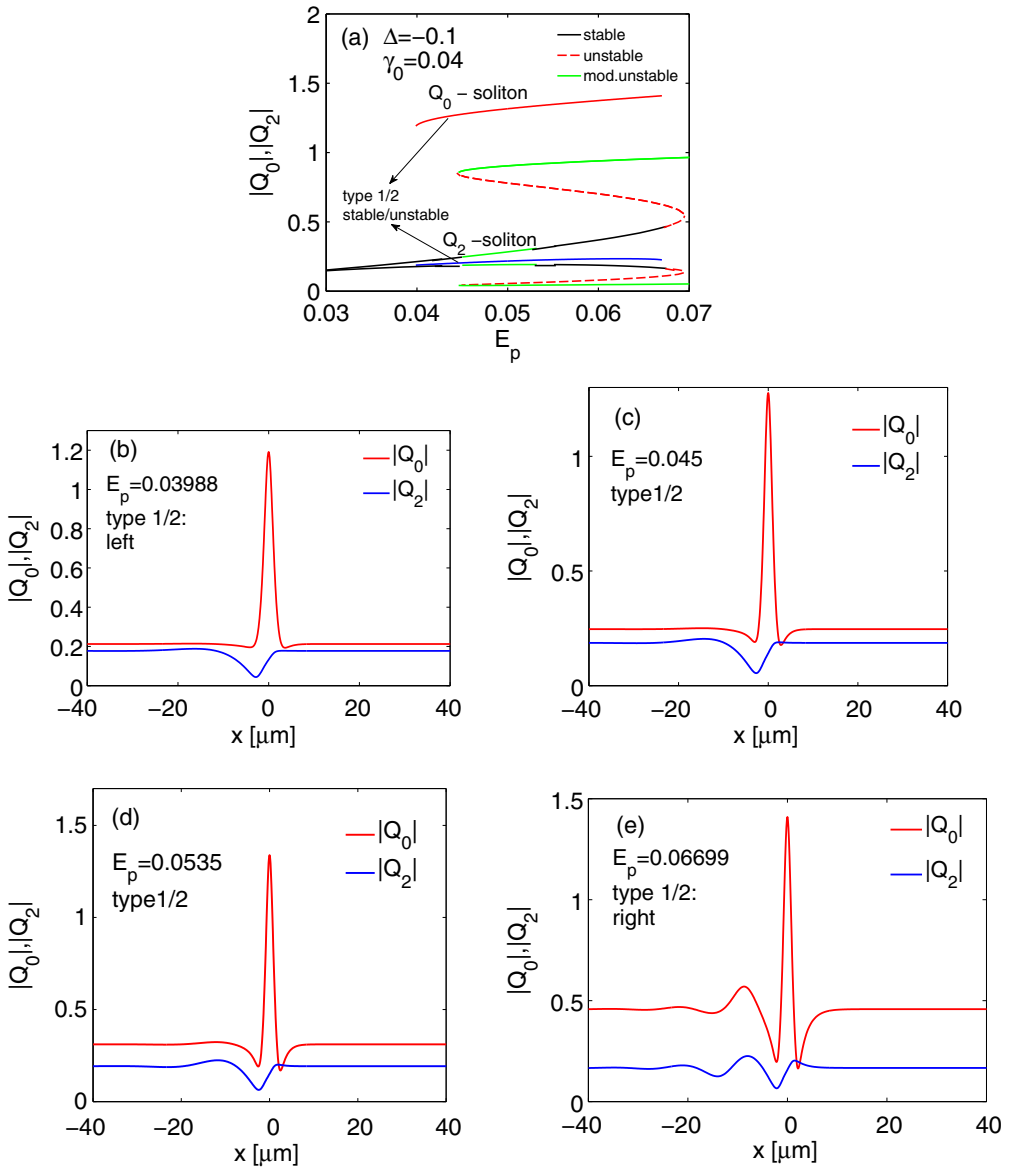


FIG. 4. (a) Coupled stable/unstable soliton branches vs $E_p$, superimposed on the homogeneous stationary solution multistability curves (stability indicated) at $\Delta = -0.1$ and $\gamma_0 = 0.04$. (b) Stable/unstable type1 soliton profiles at the left edge of the soliton branch at $E_p = 0.03988$; (c) at $E_p = 0.045$ at the edge of the homogeneous solution stable region (black curve); (d) at $E_p = 0.0535$. (e) Stable/unstable type1 profiles at the right edge of the soliton branch at $E_p = 0.06699$.

soliton, shown in Figs. 7(a) and 7(b) at $E_p = 0.0672$, persisting up to a pump amplitude of $E_p = 0.0692$, at which point the soliton peak splits up. The splitting between the two soliton peaks becomes larger and larger with increasing the pump amplitude, eventually resulting in a well defined double-hump soliton [Figs. 7(c) and 7(d)].

The single/double-hump soliton branches are obtained from the time-dependent solution from the maximum through the soliton core and a slice through the soliton tail of the integrated power, $P_\Psi = \iint |\Psi(x,y)|^2 dxdy$, shown in Fig. 8. The transition between the single- and double-hump solitons is clearly seen from the stepwise soliton branches curves, shown in magenta. The single-hump soliton persists up to the first maximum in the soliton branch curve, above which a double-hump soliton forms.

### A. Reconstruction of the full model 2D soliton from stable type 1 soliton $Q_0$ and $Q_2$ profiles

To assess the extent to which our reduced model captures the 2D soliton dynamics, we reconstruct the 2D soliton from the obtained 1D coupled $(Q_0, Q_2)$ soliton profiles, using Eqs. (4) and plot it in Fig. 9.

We compare the reconstructed 2D solitons at $\Delta = 0, \gamma_0 = 0.04$ for the $E$ field and $\Psi$ fields with the full-model solutions, shown in Figs. 9(a)–9(d). Both solitons exhibit the characteristic two-fold split tail which can be considered as a signature of the zero-detuning case (cf. Fig. 4 of Ref. [36]). We note that the full-model soliton [Figs. 9(c) and 9(d)] is more strongly localized in a transverse direction ($y$ axis) compared to the reconstructed one, obtained from the reduced model [Figs. 9(a) and 9(b)]. This is expected as our reduced model

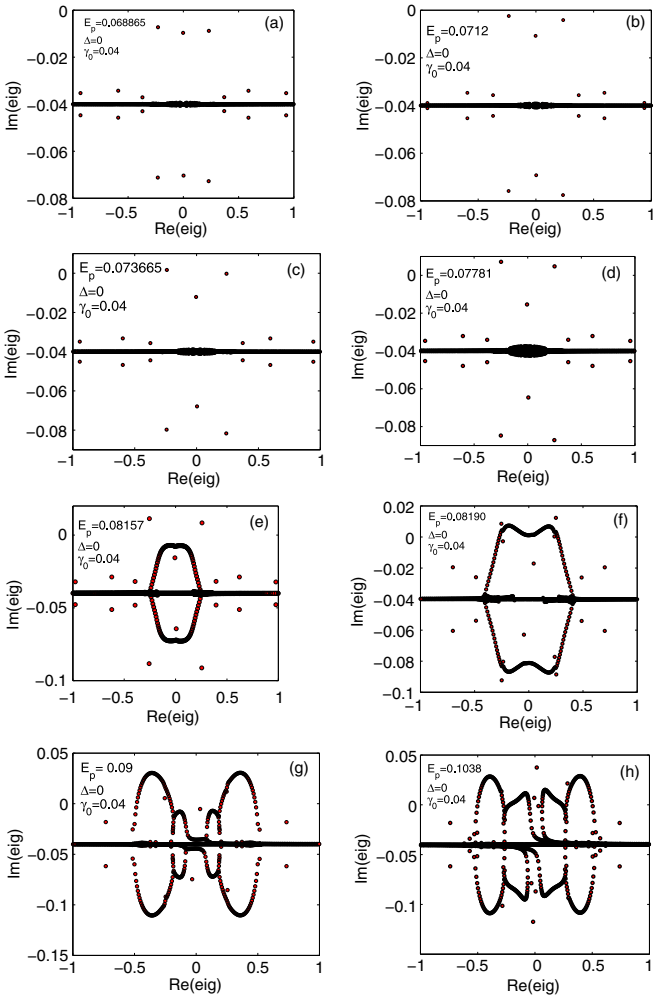


FIG. 5. Full eigenvalue spectrum of the soliton branch [Fig. 3(a)] $\Delta = 0, \gamma_0 = 0.04$: (a) at $E_p = 0.068865$; (b) at $E_p = 0.0712$: the solitons are stable for these pump amplitudes [$\lambda = Im(eig) < 0$]. Unstable solitons (at least one $\lambda > 0$): (c) at the right edge of type1 stable soliton branch at $E_p = 0.073665$; (d) at $E_p = 0.07781$ (left edge of unstable soliton branch); (e) at $E_p = 0.08157$: right edge before kink; (f) at $E_p = 0.08190$ after kink; (g) $E_p = 0.09$ middle of unstable soliton branch; (h) at $E_p = 0.1038$: right edge of unstable soliton branch.

assumes an unchanged transverse mode along the $y$ direction. The unstable soliton (type 2) profiles are shown for comparison in Figs. 9(e) and 9(f). The reconstructed and full-model 2D solitons for $\Delta = -0.1$ and $\gamma_0 = 0.04$ are displayed in Fig. 10. Comparison between the reconstructed, Figs. 10(a) and 10(b), and the full-model 2D solitons, Figs. 10(c) and 10(d), at the left soliton branch edge reveals a similar type of solitons with a simpler shape and a single-lobe tail. Similar to the previous case considered, the full-model solitons exhibit stronger localization in a transverse direction to the propagation, showing again the limitations of our reduced model. The reconstructed soliton profiles at the right edge of the soliton branch in Figs. 10(e) and 10(f) are quite similar to the full-model ones, Figs. 10(g) and 10(h), both exhibiting tail oscillations and a stronger transverse localization in the case of the full-model solitons.

### B. Projection of full-model solutions

In the previous section we compared the reconstructed 2D soliton profiles from our reduced model with the full-model 2D dynamical solution. To complete our comparison both ways, we compare the projections of the final full-model dynamically evolved profile, as computed from Eqs. (1) and (2) onto mode 0,2,4, using the inverse transformation [Eqs. (4)] thereby reconstructing $Q_0$, $Q_2$, and $Q_4$ soliton components. The reconstructed components for $\Delta = 0, \gamma = 0.04$ are shown in Fig. 11 for pump amplitudes $E_p = 0.0672, 0.0732$.

Note that all soliton components at a pump amplitude $E_p = 0.0672$ exhibit a single peak and thus correspond to a single-hump soliton [cf. Figs. 7(a) and 7(b)]. By contrast, the soliton components at $E_p = 0.0732$ exhibit double peaks, as expected for double-hump solitons [cf. Figs. 7(c) and 7(d)]. Note that the $Q_4$ soliton component is small compared to $Q_2$, which justifies our modal expansion method.

The reconstructed soliton branches for $\Delta = 0, \gamma_0 = 0.04$, computed as $max|Q_j|, j = 0,2,4$ from the full model, using the inverse transformation [Eqs. (4)], are shown in Fig. 3(a) with connected (by a magenta line) open circles, superimposed on the homogeneous solution background of the reduced model and the soliton branches, inferred from the reduced model. A comparison between the soliton branches obtained by our reduced model and the ones obtained by projection of the fully evolved 2D soliton from the dynamical model shows remarkable agreement between the $Q_2$ components both in amplitude and domain of soliton existence (excluding the points corresponding to double-hump solitons on the soliton projection branch). The $Q_0$ components match in domains of soliton existence but differ in amplitude. We attribute this difference to transverse localization effects absent in the reduced model.

### C. Domains of soliton existence

Finally we perform a comparison between the domain of stable type 1 soliton existence for the zero-detuning case ($\Delta = 0, \gamma_0 = 0.04$) with the soliton branch computed by a 2D Newton-Raphson method (cf. shaded area in Fig. 2(c) [36]). Both soliton branches are superimposed on the homogeneous solutions and the full-model multistability curve (black dash-dotted line) in Fig. 12. The 2D Newton method-inferred soliton branch is computed as a $max|E|$ and is shown in cyan. The full-model 2D Newton-inferred soliton branch and our reduced model branches are in excellent agreement, thus confirming the soliton existence domain computed in Ref. [36].

The open circle points in the gap between the stable (type 1) and unstable (type 2) solitons are computed by solving the time-dependent equations for the coupled $(Q_0, Q_2)$ soliton [Eqs. (A1) and (A3)]. We should note that although the dynamical model converges to these solutions, we were unable to connect them by Newton method to either the unstable or stable soliton branches. As these solutions happen to be in a range of pump amplitudes where the multihumped solitons have been predicted by the full model, we attribute these solutions to multihump solitons. This bifurcation behavior deserves further investigation but will be the subject of a further study. Our reduced model reproduces remarkably well

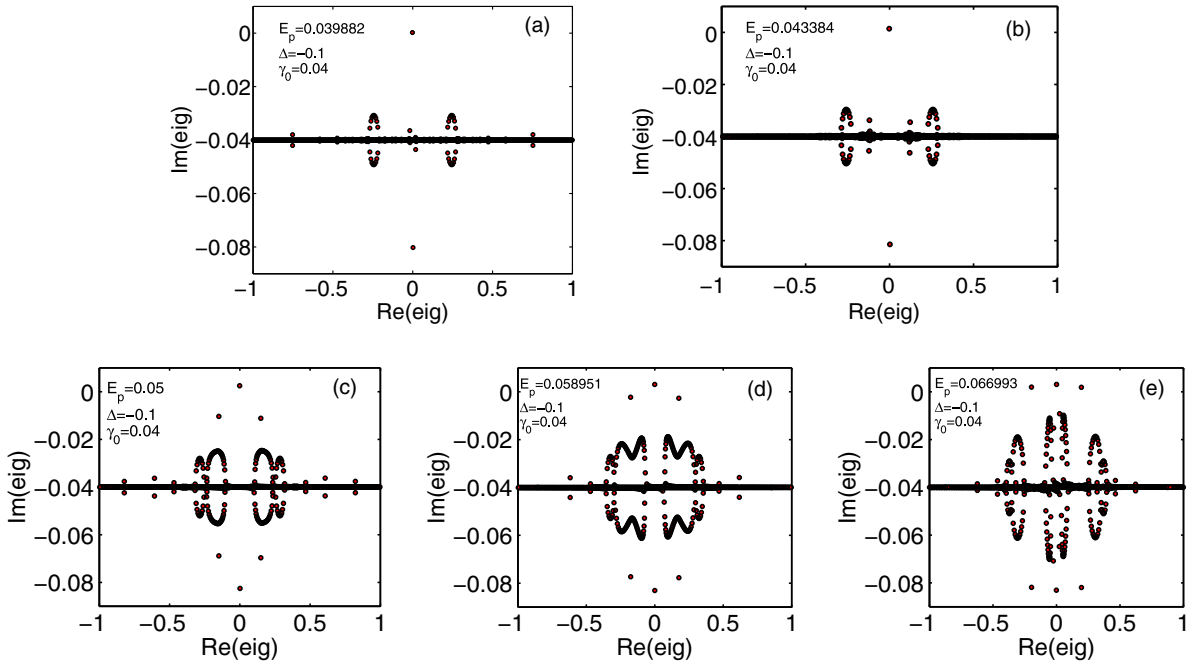


FIG. 6. Full eigenvalue spectrum for the soliton branch [Fig. 4(a)] at $\Delta = -0.1, \gamma_0 = 0.04$ at the: (a) left edge $E_p = 0.039882$; (b) right edge of the homogeneous stable solution background $E_p = 0.043384$; (c) at $E_p = 0.05$; (d) right edge of modulationally unstable background region $E_p = 0.058951$; (e) right edge of soliton branch $E_p = 0.066993$; the solitons are slightly unstable for all pump amplitudes ($\lambda \approx 0 > 0$).

the soliton existence domain, computed from the full model by 2D Newton method [36].

## V. CONCLUSION

We have developed a 1D reduced model, based on modal expansion of our full 2D mean-field model polariton solutions in a microcavity wire, which allows us to analyze the intermodal interactions and introduce externally controllable parameters. We demonstrated that by considering just two coupled modes (fundamental and the second-order microcavity wire modes), we can correctly reproduce the onset of spatial multistability upon variation of pump detuning. Furthermore, we show that a simplified 1D coupled-mode model is sufficient to reproduce the stable soliton existence domain of the full model and thus provide guidance for experiments.

Our simplified 1D approach has limitations, as the expansion in linear modes is currently truncated to the second-order term, and to achieve a more rigorous description of the mode reshaping and nonlinear self-defocusing effects in the transverse direction, formally taken into account by the

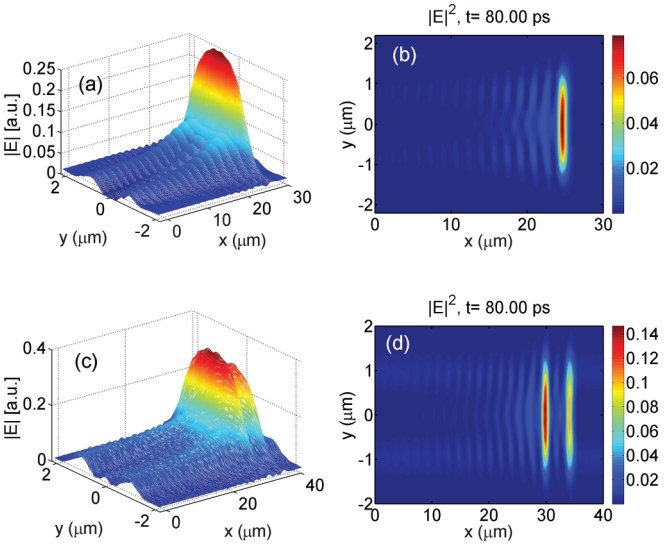


FIG. 7. Snapshot at $t = 80$ps of a (a),(b) single-hump soliton for $E_p = 0.0672$, $Es = 0.34114$; (c),(d) double-hump soliton for $E_p = 0.0762$, $Es = 0.34114$ at $\Delta = 0$.

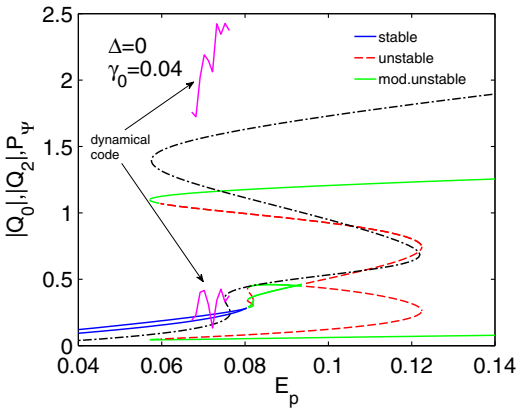


FIG. 8. Soliton branch inferred from dynamical computation of Eqs. (1) and (2) superimposed on the coupled multistability curves of the reduced model and the full model (black dash-dotted curve) at $\Delta = 0, \gamma_0 = 0.04$: single-hump solitons persist up to the first maximum, above which double-hump solitons are formed.

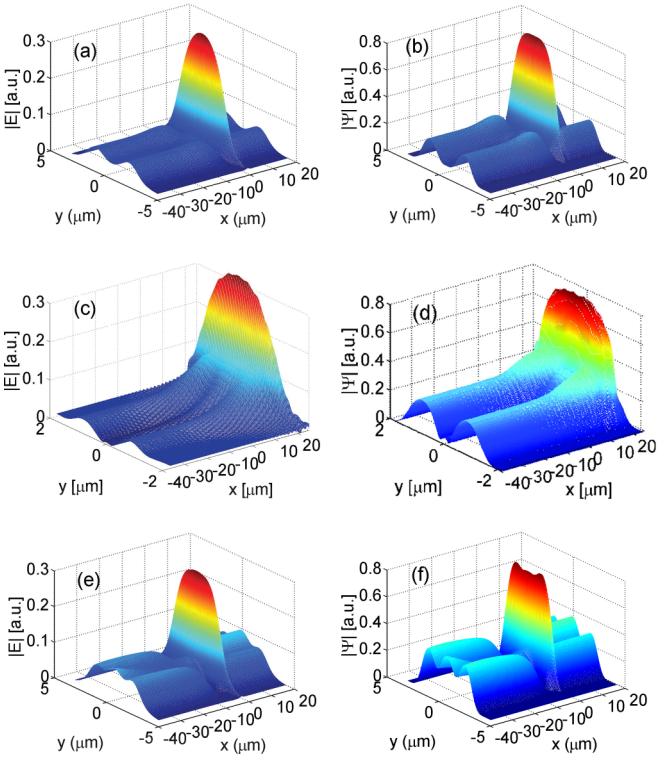


FIG. 9. 3D plot of the reconstructed 2D soliton at $\Delta = 0, \gamma_0 = 0.04$ (see Fig. 3): (a) $|E|$; (b) $|\Psi|$ from type 1 stable soliton $(Q_0, Q_2)$ profiles at $E_p = 0.0715$; (c),(d) full-model soliton solutions [Eqs. (1) and (2)] at $E_p = 0.0715$; (e),(f) reconstructed $|E|$ and $|\Psi|$ 3D plots from the unstable type 2 soliton at $E_p = 0.08572$.

correction terms $\vec{B}_j$ in the perturbation expansion, they need to be calculated in the next order of the perturbation theory.

This simplified model can be used as a framework for analysis of the complex spatio-temporal dynamics of multimode polariton solitons in microcavity wires and of effects, such as, e.g., nonmonotonous wire width dependence of the soliton existence domains, which becomes entangled and cannot be understood on the basis of the full mean-field model. Similar to single-mode solitons, coupled-mode solitons could provide a powerful concept for description of the complex nonlinear polariton dynamics in confined microcavity structures. Understanding the complex dynamical nonlinear soliton formation phenomena within the coupled-mode picture would be of great importance for practical realization of the future integrated polaritonic devices, based on structured microcavities, with microcavity wires acting as basic functional components. We note that in order to fully elucidate the nonlinear polariton dynamics, further work is needed to investigate conditions of formation and stability of multihump solitons in this confined system which will be a subject of a future study.

## ACKNOWLEDGMENTS

We acknowledge helpful discussions with D. V. Skryabin. G.S. acknowledges funding through the Leverhulme Trust Research Project Grant No. RPG-2012-481. A.V.G. acknowledges EU Network Project LIMACONA (Project No. 612600) and A.P. acknowledges the support of SFB 787 of the DFG.

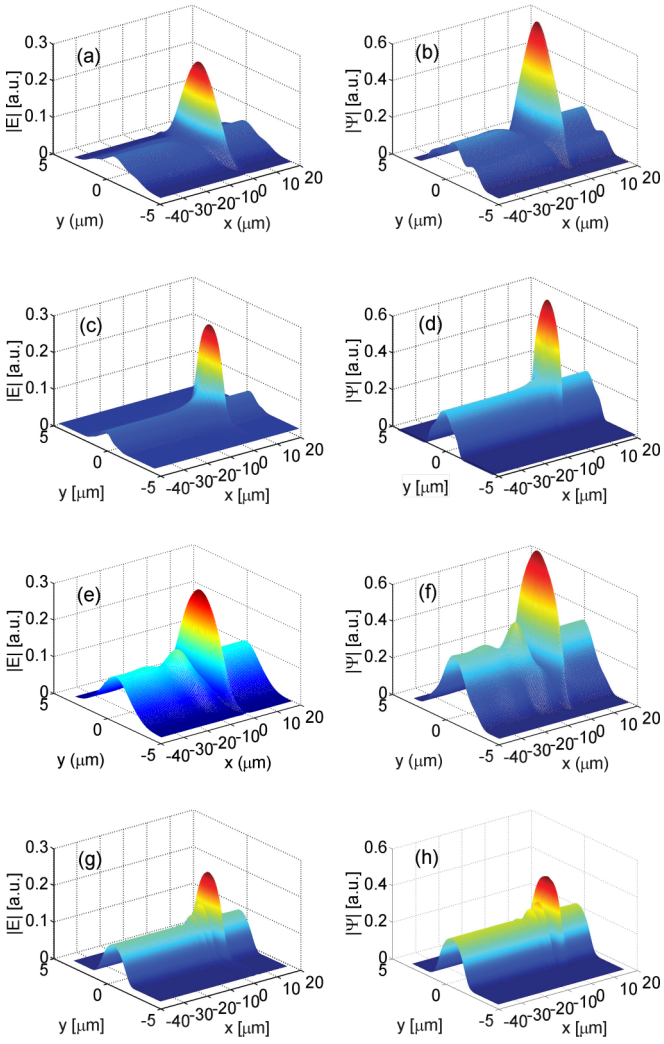


FIG. 10. 3D plot of the reconstructed 2D soliton at $\Delta = -0.1$, $\gamma_0 = 0.04$ (a) $|E|$; (b) $|\Psi|$ from type 1/2 stable/unstable soliton $(Q_0, Q_2)$ profiles (see Fig. 4) at the (a) left edge of the soliton branch $E_p = 0.03988$. (c),(d) Full-model 2D soliton solutions [Eqs. (1) and (2)] for at the left edge; (e, f) Reconstructed solitons at the right edge of the soliton branch for $E_p = 0.067$; (g,h) Full-model 2D solitons at the right edge of the soliton branch.

## APPENDIX A: THREE COUPLED MODES

Consider three coupled modes ($j = 0,1,2$) and introduce linear operators: $\hat{\mathcal{L}}_j = \Delta - \omega_{j0} + i\gamma_0 + i\omega_{j1}\partial_x + \frac{\omega_{j2}}{2}\partial_x^2$. Owing to the mode symmetry there are only a few nonvanishing nonlinear coefficients, $\Gamma_{lmn,j}$ and with the chosen normalization, $\Gamma_{jk} = \Gamma_{kj}$. The full system can be written as:

$$\begin{aligned} i\partial_t Q_0 + \hat{\mathcal{L}}_0 Q_0 = {} & ih_0 + (\Gamma_{00}|Q_0|^2 + 2\Gamma_{10}|Q_1|^2 \\ & + 2\Gamma_{20}|Q_2|^2)Q_0 + \Gamma_{002,0}\big(2|Q_0|^2 Q_2 \\ & + Q_0^2 Q_2^*\big) + \Gamma_{112,0}\big(2|Q_1|^2 Q_2 + Q_1^2 Q_2^*\big) \\ & + \Gamma_{222,0}|Q_2|^2 Q_2 \qquad \text{(A1)} \\ i\partial_t Q_1 + \hat{\mathcal{L}}_1 Q_1 = {} & ih_1 + (\Gamma_{11}|Q_1|^2 + 2\Gamma_{01}|Q_0|^2 \\ & + 2\Gamma_{21}|Q_2|^2)Q_1 \qquad \text{(A2)} \end{aligned}$$

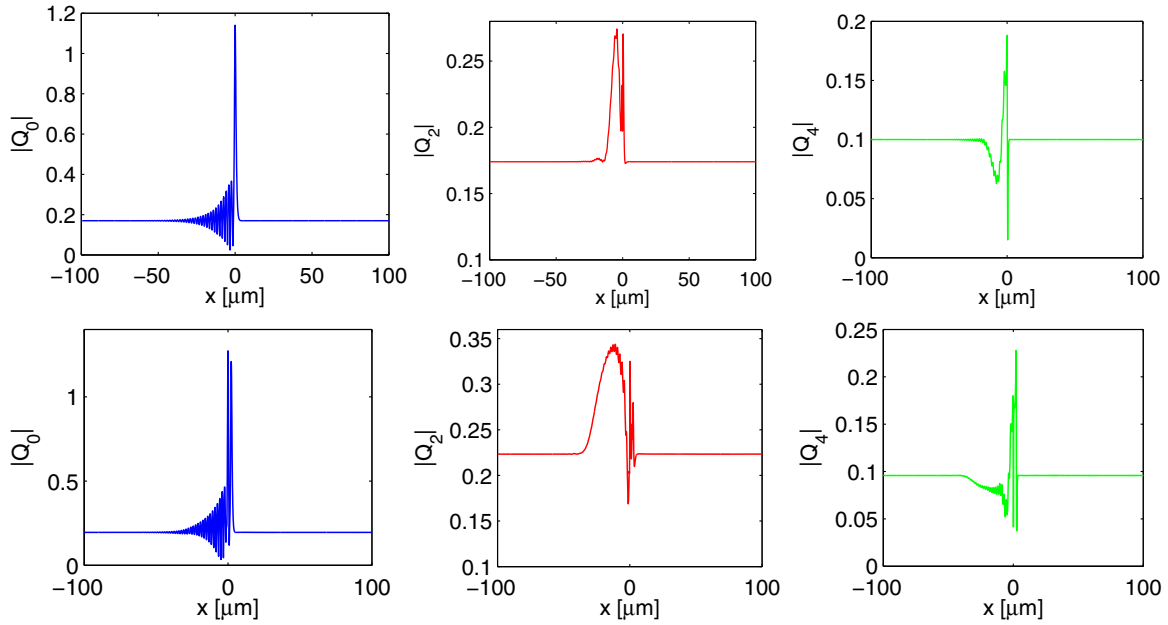


FIG. 11. Reconstructed $Q_0$, $Q_2$, and $Q_4$ soliton components from final evolved full-model $(E,\Psi)$ solutions at $\Delta = 0, \gamma_0 = 0.04$, using inverse transform [Eq. (4)]: upper row—$E_p = 0.0672$, corresponding to a single-hump soliton; lower row—$E_p = 0.0732$, corresponding to a double-hump soliton.

$$i\partial_t Q_2 + \hat{\mathcal{L}}_2 Q_2 = ih_2 + (\Gamma_{22}|Q_2|^2 + 2\Gamma_{02}|Q_0|^2 + 2\Gamma_{12}|Q_1|^2)Q_2 + \Gamma_{220,2}\big(2|Q_2|^2 Q_0 + Q_2^2 Q_0^*\big) + \Gamma_{110,2}\big(2|Q_1|^2 Q_0 + Q_1^2 Q_0^*\big) + \Gamma_{000,2}|Q_0|^2 Q_0. \quad \text{(A3)}$$

Rescaling the $x$ coordinate and transforming into moving frame: $\xi = \frac{1}{\sqrt{|\omega_{02}|}}(x - \omega_{01}t)$, the linear operators become:

$$\hat{\mathcal{L}}_0 = \Delta - \omega_{00} + i\gamma_0 + \frac{d_0}{2}\partial_\xi^2, \quad \text{(A4)}$$

$$\hat{\mathcal{L}}_1 = \Delta - \omega_{10} + i\gamma_0 + iv_1\partial_\xi + \frac{d_1}{2}\partial_\xi^2, \quad \text{(A5)}$$

$$\hat{\mathcal{L}}_2 = \Delta - \omega_{20} + i\gamma_0 + iv_2\partial_\xi + \frac{d_2}{2}\partial_\xi^2, \quad \text{(A6)}$$

where

$$v_j = \frac{\omega_{j1} - \omega_{01}}{\sqrt{|\omega_{02}|}}, \quad \text{(A7)}$$

$$d_j = \frac{\omega_{j2}}{|\omega_{02}|} \quad (d_0 = \pm 1), \quad \text{(A8)}$$

where $v_j$ is the relative group velocity of the $j$th mode with respect to the fundamental mode velocity.

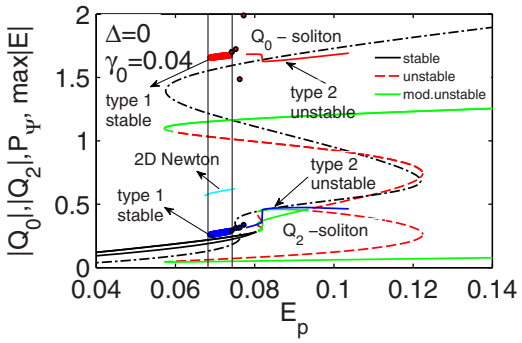


FIG. 12. Soliton branches of type 1 stable and type 2 unstable solitons at $\Delta = 0, \gamma_0 = 0.04$ superimposed on the coupled multistability $(Q_0, Q_2)$ curves of the reduced model and the multistability curve ($P_\Psi = \int |\Psi|^2 dy$ vs $E_p$) full model (black dash-dotted curve). The domain of stable soliton existence is indicated by a rectangle. The soliton branch ($max|E|$) computed by 2D Newton-Raphson method for the full model is shown for comparison. The points correspond to soliton solutions that cannot be connected to the stable branch, since they represent multihump soliton solutions.

## APPENDIX B: PARAMETER SET FOR THE MICROCAVITY WIRE

We choose all parameters as in Ref. [36]. In Fig. 1(b) dispersions of the energetically lowest-lying three lower polariton branches are plotted, along with their parabolic fits, giving:

$$\omega_{00} = -0.2583, \quad \omega_{01} = 0.3311, \quad \omega_{02} = -0.3129, \quad \text{(B1)}$$

$$\omega_{10} = -0.1731, \quad \omega_{11} = 0.2134, \quad \omega_{12} = -0.1693, \quad \text{(B2)}$$

$$\omega_{20} = -0.0922, \quad \omega_{21} = 0.1172, \quad \omega_{22} = -0.0647, \quad \text{(B3)}$$

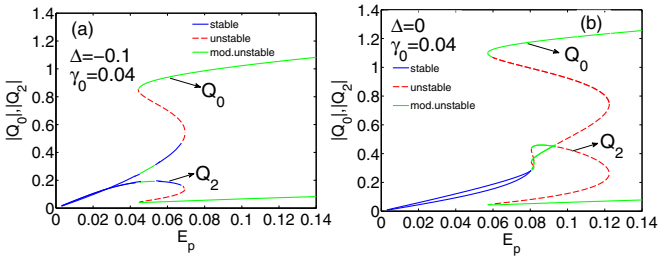


FIG. 13. Stability analysis of the homogeneous solution for (a) $\Delta = -0.1, \gamma_0 = 0.04$; (b) $\Delta = 0, \gamma_0 = 0.04$. Solid blue, dashed red, and solid green curves correspond to stable, unstable, and modulationally unstable branches, respectively.

and the higher-order dispersion coefficients:

$$v_1 = -0.2103, \quad v_2 = -0.3823, \tag{B4}$$

$$d_0 = -1, \quad d_1 = -0.5409, \quad d_2 = -0.2067. \tag{B5}$$

The corresponding modes are displayed in Fig. 1(c). Some nonlinear coefficients (for two coupled modes) are listed below:

$$\Gamma_{00} = 0.2111, \quad \Gamma_{11} = 0.2312, \quad \Gamma_{22} = 0.2443, \tag{B6}$$

$$\Gamma_{01} = \Gamma_{10} = 0.1481, \tag{B7}$$

$$\Gamma_{02} = \Gamma_{20} = 0.1543, \tag{B8}$$

$$\Gamma_{12} = \Gamma_{21} = 0.1568 \tag{B9}$$

$$\Gamma_{000,2} = \Gamma_{002,0} = 0.0750, \quad \Gamma_{222,0} = \Gamma_{220,2} = 0.0054, \tag{B10}$$

$$\Gamma_{112,0} = \Gamma_{110,2} = -0.0764, \tag{B11}$$

The pump coefficients are (for $q_y = 0$):

$$h_0 = E_p \cdot 0.7709, \tag{B12}$$

$$h_1 = 0, \tag{B13}$$

$$h_2 = E_p \cdot (-0.2208). \tag{B14}$$

## APPENDIX C: STABILITY ANALYSIS OF THE STATIONARY HOMOGENEOUS SOLUTION

We perform stability analysis of the stationary homogeneous nonlinear solution, adding small perturbations to the modal profiles: $Q_0 = A + \epsilon_f e^{iqx} e^{(\lambda - i\delta)t} + \epsilon_b^* e^{-iqx} e^{(\lambda + i\delta)t}$, $Q_2 = B + p_f e^{iqx} e^{(\lambda - i\delta)t} + p_b^* e^{-iqx} e^{(\lambda + i\delta)t}$ with $q, \delta, \lambda$ all real. Introducing linear operators, $\hat{\mathcal{L}}_{0,2}$ without spatial derivatives, and $\vec{\mathbf{x}} = [\varepsilon_f, \varepsilon_b, p_f, p_b]^T$, the resulting eigenvalue problem reads:

$$(\delta + i\lambda)\vec{x} = \begin{bmatrix} -\hat{\mathcal{L}}_0 & \Gamma_{00}A^2 & 2\Gamma_{20}AB^* & 2\Gamma_{20}AB \\ -\Gamma_{00}(A^*)^2 & \hat{\mathcal{L}}_0^* & -2\Gamma_{20}A^*B^* & -2\Gamma_{20}A^*B \\ 2\Gamma_{02}A^*B & 2\Gamma_{02}AB & -\hat{\mathcal{L}}_2 + v_2 q + 2(\Gamma_{22}|B|^2 + \Gamma_{02}|A|^2) & \Gamma_{22}B^2 \\ -2\Gamma_{02}A^*B^* & -2\Gamma_{02}AB^* & -\Gamma_{22}(B^*)^2 & \hat{\mathcal{L}}_2^* + v_2 q - 2(\Gamma_{22}|B|^2 + \Gamma_{02}|A|^2) \end{bmatrix} \vec{x}, \tag{C1}$$

The eigenvalues and eigenvectors are found numerically and the stable ($\lambda < 0$), unstable($\lambda(q = 0) > 0$), and modulationally unstable ($\lambda > 0$ only for some $q \neq 0$) branches of the multistability curves for $Q_0$ and $Q_2$ nonlinear homogeneous solutions are plotted against pump amplitude $E_p$ for $\Delta = 0, -0.1$ and $\gamma_0 = 0.04$ in Fig. 13.


[1] J. L. O'Brien, A. Furusawa, and J. Vučković, Nat. Photon. **3**, 687 (2009).

[2] V. M. Menon, L. I. Deych, and A. A. Lisyanski, Nat. Photon. **4**, 345 (2010).

[3] T. C. H. Liew, A. V. Kavokin, and I. A. Shelykh, Phys. Rev. Lett. **101**, 016402 (2008).

[4] A. Amo, T. C. H. Liew, C. Adrados, R. Houdré, E. Giacobino, A. V. Kavokin, and A. Bramati, Nat. Photon. **4**, 361 (2010).

[5] P. G. Savvidis, J. J. Baumberg, R. M. Stevenson, M. S. Skolnick, D. M. Whittaker, and J. S. Roberts, Phys. Rev. Lett. **84**, 1547 (2000).

[6] R. M. Stevenson, V. N. Astratov, M. S. Skolnick, D. M. Whittaker, M. Emam-Ismail, A. I. Tartakovskii, P. G. Savvidis, J. J. Baumberg, and J. S. Roberts, Phys. Rev. Lett. **85**, 3680 (2000).

[7] A. Kavokin, J. Baumberg, G. Malpuech, and F. Laussy, *Microcavities* (Oxford University Press, Oxford, 2007).

[8] H. Deng, H. Haug, and Y. Yamamoto, Rev. Mod. Phys. **82**, 1489 (2010).

[9] M. Sich, D. N. Krizhanovskii, M. S. Skolnick, A. V. Gorbach, R. Hartley, D. V. Skryabin, E. A. Cerda-Méndez, K. Biermann, R. Hey, and P. V. Santos, Nat. Photon. **6**, 50 (2012).

[10] A. Amo, S. Pigeon, D. Sanvitto, V. G. Sala, R. Hivet, I. Carusotto, F. Pisanello, G. Leménager, R. Houdré, E. Giacobino, C. Ciuti, and A. Bramati, Science **332**, 1167 (2011).

[11] A. Amo, D. Sanvitto, F. P. Laussy, D. Ballarini, E. del Valle, M. D. Martin, A. Lemaître, J. Bloch, D. N. Krizhanovskii, M. S. Skolnick, C. Tejedor, and L. Viña, Nature **457**, 291 (2009).

[12] V. Ardizzone, P. Lewandowski, M. H. Luk, Y. C. Tse, N. H. Kwong, A. Lücke, M. Abbarchi, E. Baudin, E. Galopin, J. Bloch, Aristide Lemaitre, P. T. Leung, Ph. Roussignol, R. Binder, J. Tignon, and S. Schumacher, Scientific Reports **3**, 1 (2013).

[13] N. H. Kwong, R. Takayama, I. Rumyantsev, M. J. Kuwata-Gonokami, and R. Binder, Phys. Rev. B **64**, 045316 (2001).

[14] G. Nardin, G. Grosso, Y. Léger, B. Pietka, F. Mirier-Genoud, and B. Deveaud-Plédran, Nat. Phys. **7**, 635 (2011).
[15] K. G. Lagoudakis, M. Wouters, M. Richard, A. Baas, I. Carusotto, R. André, Le Si Dang, and B. Deveaud-Plédran, Nat. Phys. **4**, 706 (2008).
[16] D. Sanvitto, S. Pigeon, A. Amo, D. Ballarini, M. De Giorgi, I. Carusotto, R. Hivet, F. Pisanello, V. G. Sala, P. S. S. Guimaraes, R. Houdré, E. Giacobino, C. Ciuti, A. Bramati, and G. Gigli, Nat. Photon. **5**, 610 (2011).
[17] S. Pigeon, I. Carusotto, and C. Ciuti, Phys. Rev. B **83**, 144513 (2011).
[18] D. V. Karpov, I. G. Savenko, H. Flayac, and N. N. Rosanov, Phys. Rev. B **92**, 075305 (2015).
[19] E. A. Ostrovskaya, J. Abdullaev, A. S. Desyatnikov, M. D. Fraser, and Yu. S. Kivshar, Phys. Rev. A **86**, 013636 (2012).
[20] A. Baas, J. P. Karr, H. Eleuch, and E. Giacobino, Phys. Rev. A **69**, 023809 (2004).
[21] N. A. Gippius, I. A. Shelykh, D. D. Solnyshkov, S. S. Gavrilov, Yuri G. Rubo, A. V. Kavokin, S. G. Tikhodeev, and G. Malpuech, Phys. Rev. Lett. **98**, 236401 (2007).
[22] S. S. Gavrilov, N. A. Gippius, S. G. Tikhodeev, and V. D. Kulakovskii, J. Exp. Theor. Phys. **110**, 825 (2010).
[23] D. V. Vishnevsky, D. D. Solnyshkov, N. A. Gippius, and G. Malpuech, Phys. Rev. B **85**, 155328 (2012).
[24] O. Bozat, I. G. Savenko, and I. A. Shelykh, Phys. Rev. B **86**, 035413 (2012).
[25] T. K. Paraïso, M. Wouters, Y. Léger, F. Mourier-Genoud, and B. Deveaud-Plédran, Nat. Mater. **9**, 655 (2010).
[26] C. Adrados, A. Amo, T. C. H. Liew, R. Hivet, R. Houdré, E. Giacobino, A. V. Kavokin, and A. Bramati, Phys. Rev. Lett. **105**, 216403 (2010).
[27] R. Cerna, Y. Léger, T. K. Paraïso, M. Wouters, F. Morier-Genoud, M. T. Portella-Oberli, and B. Deveaud, Nat. Commun. **4**, 2008 (2013).
[28] S. S. Gavrilov, A. V. Sekretenko, N. A. Gippius, C. Schneider, S. Höfling, M. Kamp, A. Forchel, and V. D. Kulakovskii, Phys. Rev. B **87**, 201303 (2013).
[29] H. Abbaspour, G. Sallen, S. Trebaol, F. Morier-Genoud, M. T. Portella-Oberli, and B. Deveaud, Phys. Rev. B **92**, 165303 (2015).
[30] E. Cancellieri, F. M. Marchetti, M. H. Szymańska, and C. Tejedor, Phys. Rev. B **83**, 214507 (2011).
[31] O. Kyriienko, E. A. Ostrovskaya, O. A. Egorov, I. A. Shelykh, and T. C. H. Liew, Phys. Rev. B **90**, 125407 (2014).
[32] M. De Giorgi, D. Ballarini, E. Cancellieri, F. M. Marchetti, M. H. Szymanska, C. Tejedor, R. Cingolani, E. Giacobino, A. Bramati, G. Gigli, and D. Sanvitto, Phys. Rev. Lett. **109**, 266407 (2012).
[33] M. Brambilla, L. A. Lugiato, V. Penna, F. Prati, C. Tamm, and C. O. Weiss, Phys. Rev. A **43**, 5114 (1991).
[34] C. Ouellet-Plamondon, G. Sallen, F. Morier-Genoud, D. Y. Oberli, M. T. Portella-Oberli, and B. Deveaud, Phys. Rev. B **93**, 085313 (2016).
[35] M. Wouters, T. K. Paraïso, Y. Léger, R. Cerna, F. Morier-Genoud, M. T. Portella-Oberli, and B. Deveaud-Plédran, Phys. Rev. B **87**, 045303 (2013).
[36] G. Slavcheva, A. V. Gorbach, A. Pimenov, A. G. Vladimirov, and D. V. Skryabin, Opt. Lett. **40**, 1787 (2015).
[37] E. Wertz, L. Ferrier, D. D. Solnyshkov, R. Johne, D. Sanvitto, A. Lemaître, I. Sagnes, R. Grousson, A. V. Kavokin, P. Senellart, G. Malpuech, and J. Bloch, Nat. Phys. **6**, 860 (2010).
[38] M. H. Luk, Y. C. Tse, N. H. Kwong, P. T. Leung, P. Lewandowski, R. Binder, and S. Schumacher, Phys. Rev. B **87**, 205307 (2013).
[39] O. A. Egorov, A. Werner, T. C. H. Liew, E. A. Ostrovskaya, and F. Lederer, Phys. Rev. B **89**, 235302 (2014).
[40] G. Slavcheva, A. V. Gorbach, and A. Pimenov [J. Optics (to be published)].
[41] E. Wertz, L. Ferrier, D. D. Solnyshkov, P. Senellart, D. Bajoni *et al.*, Appl. Phys. Lett. **95**, 051108 (2009).
[42] L. G. Wright, D. N. Christodoulides, and F. W. Wise, Nat. Photon. **9**, 306 (2015).
[43] A. Efimov, A. J. Taylor, F. G. Omenetto, J. C. Knight, W. J. Wadsworth, and P. St. Russell, Opt. Express **11**, 910 (2003).
[44] D. Modotto, C. De Angelis, M. A. Magaña-Cervantes, R. M. De La Rue, R. Morandotti, St. Linden, H. M. van Driel, and J. St. Aitchison, J. Opt. Soc. Am. B **22**, 870 (2005).
[45] A. Hasegawa, Opt. Lett. **5**, 416 (1980).
[46] B. Crosignani and P. D. Porto, Opt. Lett. **6**, 329 (1981).
[47] B. Crisignani, A. Cutolo, and P. D. Porto, J. Opt. Soc. Am. **72**, 1136 (1982).
[48] W. H. Renninger and F. W. Wise, Nat. Commun. **4**, 1719 (2013).
[49] L. G. Wright, W. H. Renninger, D. N. Christodoulides, and F. W. Wise, Opt. Express **23**, 3492 (2015).
[50] S. Buch and G. P. Agrawal, Opt. Lett. **40**, 225 (2015).
[51] R. H. Stolen, J. E. Bjorkholm, and A. Ashkin, Appl. Phys. Lett. **24**, 308 (1974).
[52] R. H. Stolen, IEEE J. Quantum Electron. **11**, 100 (1975).